Renewable Energy 119 (2018) 754–766

Contents lists available at ScienceDirect

Renewable Energy

journal homepage: www.elsevier.com/locate/renene

Assessing progressive failure in long wind turbine blades under quasi-static and cyclic loads

Yangjie Zuo [a, b], John Montesano [c], Chandra Veer Singh [b, d, *]

[a] Department of Mechanical Engineering, Northwestern Polytechnical University, 127 Youyi Ave. West, Xi'an, 710 072, China
[b] Department of Materials Science and Engineering, University of Toronto, 184 College St., Suite 140, Toronto, M5S 3E4, Canada
[c] Mechanical & Mechatronics Engineering, University of Waterloo, 200 University Ave. West, Waterloo, N2L 3G1, Canada
[d] Department of Mechanical and Industrial Engineering, University of Toronto, 5 King's College Road, Toronto, M5S 3G8, Canada

ARTICLE INFO

Article history:
Received 7 December 2016
Received in revised form
4 October 2017
Accepted 29 October 2017
Available online 2 November 2017

Keywords:
Wind turbine blade
Multi-scale model
CZM
Fatigue progressive failure

ABSTRACT

Predicting progressive failure and consequential loss in the load-bearing capability of large-scale composite wind blades is vital for accurately assessing their service life and maintenance. A physics-based multi-scale damage model describing progressive ply cracking and joint adhesive debonding in blades under both quasi-static and cyclic loading is presented. The complete structure of the blade was considered including the shell-spar adhesive joint and shell-root adhesive joint. For quasi-static loading, the geometrical transition region of the blade was observed as the critical ply crack damage region, which was in agreement with previous experimental results. The matrix micro-cracking damage was mainly caused by high gale wind speeds, and adhesive debonding ultimately initiated at the shell-spar joint. The blade tip deflection increased nonlinearly with increasing wind speeds, reaching 29.0% of the blade length at 19 m/s. For cyclic loading, sub-critical damage grew along the length of the blade with increasing cycles, gradually increasing the normal and shear stresses in the joint adhesive layer as the crack density increased, eventually leading to local shell-spar adhesive debonding. The simulation methodology presented here will be useful for assessing the durability and increasing the safety and accuracy of service life prediction of large-scale blade structures.

1. Introduction

Wind power is a clean, relatively inexpensive and renewable energy source, which has been growing dramatically over the past few decades [1,2]. In order to capture wind energy more effectively, there exists a demand to increase the scale of wind turbines in commercial wind power generation [3]. However, as wind turbines increase in size, so do the requirements for material and structure designs of rotor blades due to the increase of blade weight and the associated gravitational load. To meet this challenge, fiber-reinforced laminated composites are widely used in large rotor blades due to their high stiffness-to-weight ratio, strength-to-weight ratio, and resistance to fatigue failure [4,5]. However, during a typical 20-year service life, multiple evolving damage modes resulting from extreme combined cyclic loads (i.e., gravitational force, centrifugal force, and aerodynamic force) can occur in rotor blades [6–8]. These damage modes typically initiate as undetectable sub-critical cracks and progress into critical damage modes that ultimately leads to catastrophic failure. It is therefore vital to predict their evolution concurrently under both quasi-static and fatigue conditions as well the consequent loss in load bearing capability of the structure in order to facilitate an improved design for rotor blades.

Typical damage modes observed in large wind turbine blades include matrix micro-cracking, cohesive joint debonding, and inter-ply delamination, which have been studied in previous reports [9–11]. Generally, matrix micro-cracking is the first to initiate in composite laminates under both quasi-static and cyclic loading conditions. This ply cracking typically does not cause the final failure but causes appreciable stiffness degradation; and to address this, a number of excellent models have been developed to evaluate stiffness loss caused by matrix micro-cracking in composite laminates. These popular methods include elasticity approach [12], continuum damage approach [13], ply discount method [14], synergistic damage mechanics approach [15,16], and damage

* Corresponding author. Department of Materials Science and Engineering, University of Toronto, 184 College St., Suite 140, Toronto, M5S 3E4, Canada.
E-mail address: chandraveer.singh@utoronto.ca (C.V. Singh).

https://doi.org/10.1016/j.renene.2017.10.103
0960-1481/

accumulation approach [17]. From the inspection of damage in composite blades, it has been revealed that matrix micro-cracking is likely caused by critical cyclic loading [11,18]. In regards to model development focused on wind turbine composites, a physically-based failure model was developed to investigate the mechanism of matrix micro-cracking in composite blades under cyclic loading [19], however, the blades were simplified as beam structures. A physics-based multi-scale progressive damage model was also developed to assess the matrix cracking evolution of the blades under quasi-static and cyclic loading, in which full-scale geometries of rotor blades were considered [20].

With regards to adhesive joint debonding, full-scale composite blade tests revealed that debonding was the main cause of rotor blade structural collapse [21,22]. The initiation of debonding was reported to be caused by voids in the adhesive layer due to the reduction of joint strength [23]. A finite element study showed that the debonding initiated and propagated progressively in the edge of the adhesive bond line according to the high shear stress in adhesive layers [24]. In addition, fatigue loads were found to have an import influence on the debonding evolution of the composite blade root joint [25]. In addition, the ensuing delamination can lead to the buckling of laminated composite materials even if at a lower level of compressive load [26,27], and the delamination and buckling coupled phenomenon of large composite blades was regarded to govern the ultimate collapse of large composite blade [21,28]. In a failure test, the delamination of a spar cap was likely responsible for the catastrophic failure of a rotor blade at the transition region due to local compressive forces [10].

The final failure of wind turbine blades is observed to involve a combination of damage modes [10,19]. In composite laminates, ply cracks can induce inter-laminar delamination cracking, which is one of the main sources of failure [29]. A high density of ply cracks is also reported to lead to localized delamination and skin/spar cap adhesive debonding in turbine blades [30]. A study of the interaction of these damage modes is vital to accurately capture the nonlinear behavior of composite wind blades under both quasi-static and fatigue loading. However, the previous studies on this topic have only modeled one damage mode of rotor blades [19,20,25,26], which limits their applicability for practical wind turbine design and durability assessment. Furthermore, the geometric models of these studies mainly represented only one component of rotor blades such as the root, and not the full structure including the root, spar and shell; clearly, an important limitation of reported results in optimizing rotor blade designs for better life-time performance. Therefore, a full-structural model considering sub-critical and critical damage modes is required to assess the durability and increase the accuracy of service life prediction of large scale blade structures.

The aim of this study is to assess the progressive damage of large composite rotor blade, considering the co-effects of matrix micro-cracking damage and joint adhesive debonding under both quasi-static and cyclic loads. Herein, the full structure of a composite blade was modeled and the details of the shell-root and shell-spar adhesive joints were included. The constitutive equations for the damaged laminates, based on a synergistic damage mechanics [15,16,20,31], were implemented as a user-defined material subroutine (UMAT) in the commercial finite element code ANSYS for the assessment of matrix micro-cracking damage. A cohesive zone model (CZM) [32–34] using contact elements was employed to predict the initiation and growth of debonding. Based on Weibull distribution of wind speeds [6], the effects of potential wind speed pressures on the progressive damage of the blade were evaluated by quasi-static and fatigue simulations. Results presented included the initiation and propagation of both matrix micro-cracking damage and adhesive debonding, moreover, the interaction of the damage and debonding was also discussed by cyclic loading cases.

2. Damage mechanics model

2.1. The progressive damage model

In order to evaluate the effect of matrix micro-cracking of rotor blades, an approach based on micromechanics and continuum damage mechanics to predict the crack density and stiffness degradation of the blades has been reported in our previous work [20]. In this approach, the stress tensor, σ_{ij}, was characterized by the strain tensor, ε_{kl}, as [15,35]:

$$\sigma_{ij} = C_{ijkl}\left(D_{ij}^{(\alpha)}(\rho)\right)\varepsilon_{kl} \tag{1}$$

where ρ represents the crack density for cracks in a given ply orientation, the defined as damage mode α. A second-order damage tensor is used to represent the damage, as [13,36]:

$$D_{ij}^{(\alpha)}(\rho) = \frac{\kappa_\alpha t_\alpha^2}{s_\alpha t} n_i n_j \tag{2}$$

where κ_α is the constraint parameter, t_α is the cracked-ply thickness, s_α is the average crack spacing, t is the total laminate thickness, and n_i ($i = 1, 2, 3$) are the crack surface normal unit vector components. For any general symmetric laminate under in-plane multiaxial loading, the stiffness tensor for a given crack density ρ is defined as:

$$C_{ijkl} = C_{ijkl}^0 - \sum_{\alpha=1}^{N} C_{ijkl}^{\alpha} = \begin{pmatrix} \frac{E_x^0}{1-\nu_{xy}^0\nu_{yx}^0} & \frac{\nu_{xy}^0 E_y^0}{1-\nu_{xy}^0\nu_{yx}^0} & 0 \\ & \frac{E_y^0}{1-\nu_{xy}^0\nu_{yx}^0} & 0 \\ \text{Symm} & & G_{xy}^0 \end{pmatrix} - \sum_{\alpha} a_\alpha D_\alpha \begin{pmatrix} 2a_1^{(\alpha)} & a_4^{(\alpha)} & 0 \\ & 2a_2^{(\alpha)} & 0 \\ \text{Symm} & & 2a_3^{(\alpha)} \end{pmatrix} \tag{3}$$

where C_{ijkl}^0 and C_{ijkl}^{α} are, respectively, the undamaged stiffness tensor of the laminate and stiffness changes caused by damage modes α. The terms $a_i^{(\alpha)}$ and D_α are, respectively, the orthotropic damage constants and effective damage parameters for all damage modes present during loading of the laminate. The constraint parameters, κ_α, and damage constants, $a_i^{(\alpha)}$, for any general symmetric laminate were computed using the micro damage mechanics procedure that utilizes finite element computations of average crack surface displacements in representative volume elements for each damage mode, as discussed in Ref. [16].

To simulate the structural degradation of the blades, an energy-based approach was employed to predict ply crack density ρ for a general multidirectional laminate under multi-axial loading, as reported in our previous work [15]. Considering both crack opening (Mode *I*) and crack sliding (Mode *II*), new cracks are assumed to form when:

$$\left(\frac{w_I}{G_{Ic}}\right) + \left(\frac{w_{II}}{G_{IIc}}\right)^2 \geq 1 \tag{4}$$

where w_I and w_{II} represent the work required to close the new

cracks in Mode *I* and Mode *II*, respectively; and G_{Ic} and G_{IIc} are, respectively, the critical energy release rate in Mode *I* and Mode *II*.

For the case of fatigue loading, the resistance of material from cracking reduces as the number of cycles increase. This was described using the following empirical model to define the rates of change of G_{Ic} and G_{IIc} as a function of cycles [20]:

$$\frac{dG_{Ic}}{dn} = cG_{Ic,o}n^{c-1},\ \frac{dG_{IIc}}{dn} = cG_{IIc,o}n^{c-1} \tag{5}$$

where $G_{Ic,o}$ and $G_{IIc,o}$ denote the critical energy release rates for the virgin material in Mode *I* and Mode *II*, respectively, as defined in Eq. (4); and c and n are the ply-level constant and number of fatigue loading cycles.

2.2. The cohesive zone model

The cohesive zone model (CZM) is a powerful tool for the simulation of fracture in adhesive assemblies [37], which is able to adequately predict the initiation and propagation of debonding in adhesive structures. In this study, the bilinear CZM based on the model proposed by G. Alfano and M.A. Crisfield [38] is utilized to study the debonding in adhesive joints of the large composite blade under quasi-static and cyclic loads. The bilinear CZM adopts a softening traction–separation relation to predict debonding initiation and propagation. The damage initiation criterion of this model, involving the interaction of traction components, is defined as:

$$\left(\frac{\sigma^n}{\sigma^n_{\max}}\right)^2 + \left(\frac{\sigma^s}{\sigma^s_{\max}}\right)^2 = 1 \tag{6}$$

here, σ^n and σ^s are, respectively, the normal and tangential stress of the traction T; $\sigma^n_{\max}$ and $\sigma^s_{\max}$ are respectively the normal and tangential stress of the maximum traction $T_{\max}$. Therefore, the completion of debonding is defined by a power law based on the energy criterion:

$$\left(\frac{G^n}{G^n_c}\right)^2 + \left(\frac{G^s}{G^s_c}\right)^2 = 1 \tag{7}$$

where G^n and G^s are, respectively, the normal and tangential fracture energies at given loading; and G^n_c and G^s_c are the critical normal and tangential critical fracture energies, respectively. The debonding is described by the damage parameter d_m, which is defined as:

$$d_m = \left(\frac{\Delta_m - 1}{\Delta_m}\right)\chi \tag{8}$$

where the damage parameter $d_m = 0$ represents well bonded interface, $0 < d_m < 1$ means the initiation of debonding, and $d_m = 1$ denotes the completion of debonding; and Δ_m and χ are defined as:

$$\Delta_m = \sqrt{\left(\frac{\delta^n_i}{\delta^n_f}\right)^2 + \left(\frac{\delta^t_i}{\delta^t_f}\right)^2} \tag{9}$$

and

$$\chi = \left(\frac{\delta^n_f}{\delta^n_f - \delta^n_i}\right) = \left(\frac{\delta^t_f}{\delta^t_f - \delta^t_i}\right) \tag{10}$$

with δ^n_i and δ^n_f denoting the contact gaps at the maximum normal contact stress and at the completion of debonding, respectively; and δ^t_i and δ^t_f are tangential slip distances at the maximum tangential contact stress and at the completion of debonding, respectively.

For the bilinear CZM, damage initiation occurs when the cohesive strength is reached ($T = T_{\max}$, $\delta = \delta_i$). After the damage initiation, the debonding is assumed to be cumulative, and unloading and subsequent reloading will occur in a linear elastic manner at a more gradual slope. Finally, debonding is completed ($T = 0$, $\delta = \delta_f$) as the separation increases.

3. Finite element structural modeling

3.1. Rotor blade details

In this study, a full-structure composite blade for a 1.5 MW horizontal axis wind turbine with 70 m rotor diameter was modeled by the open source tool NuMAD [39]. This consists of upper shell, lower shell, double spar, and the root joint (see Fig. 1). The blade was modeled with a length, tip chord and reference root chord of 33.25 m, 0.875 m, and 2.8 m, respectively [20]. The spar and shell were bonded together by adhesive layers to prevent the structure buckling of the blade. The root joint, which was simplified as a cylinder with the diameter and length of 1.89 m and 0.7 m, respectively, was also bonded with the shell by adhesive layers as shown in Fig. 2. Since the blade was modeled using shell elements, the upper shell and lower shell connecting edges were treated as permanently glued interfaces.

To simplify aerodynamic loading calculations, the same airfoil section (NREL S818 [40]) was used along the blade length, which transitioned near the root to a circular section with the diameter of 1.89 m (see Fig. 1). The blade transitioned from the circular section to the NREL S818 airfoil over the span of 7.0 m, and the twist and pitch angles of the blade tip were taken as 5° and 10°, respectively [41]. Since the chord line of the tip airfoil section is parallel to the pitch angle, the tip airfoil section has no twist.

3.1.1. Blade loading

During standard operational conditions, aerodynamic, gravitational and centrifugal forces are the dominant sources of loading on the blade. As shown in Fig. 1, aerodynamic lift force, F_L, and aerodynamic drag force, F_D, depend on wind speed, v_w, local blade speed, v_b, local attack angle, α_w, and airfoil section. In this study, the aerodynamic lift and drag forces on discrete segments along the blade length were evaluated by the widely used blade element momentum (BEM) theory [42,43], and were described as:

$$F_L = \frac{1}{2}\rho v^2_{res} C_L A \tag{11}$$

$$F_D = \frac{1}{2}\rho v^2_{res} C_D A \tag{12}$$

here, C_L and C_D are the lift and drag coefficients extracted from the NREL S818 airfoil data, respectively; $\rho = 1.225$ kg/m^3 is the sea level air density; and A is the planform area of the segment obtained by:

$$A = \frac{1}{2}h(c_{upper} + c_{lower}) \tag{13}$$

where h is the segment segment length height; c_{upper} and c_{lower} are the lengths of the inboard chord and outboard chord of the segment, respectively. v_{res} is the relative resultant speed, which was calculated by:

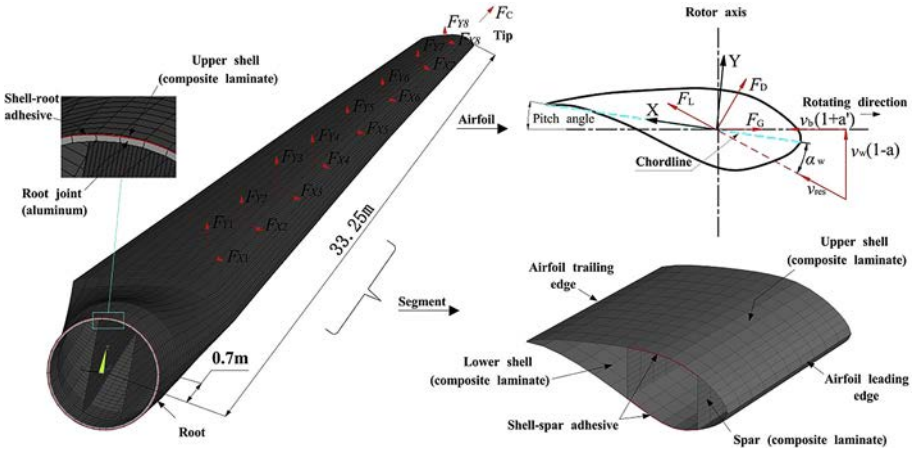

Fig. 1. Structural details and loading conditions of the FE blade model for a 1.5 MW horizontal axis wind turbine with 70 m rotor diameter modeled using NuMAD.

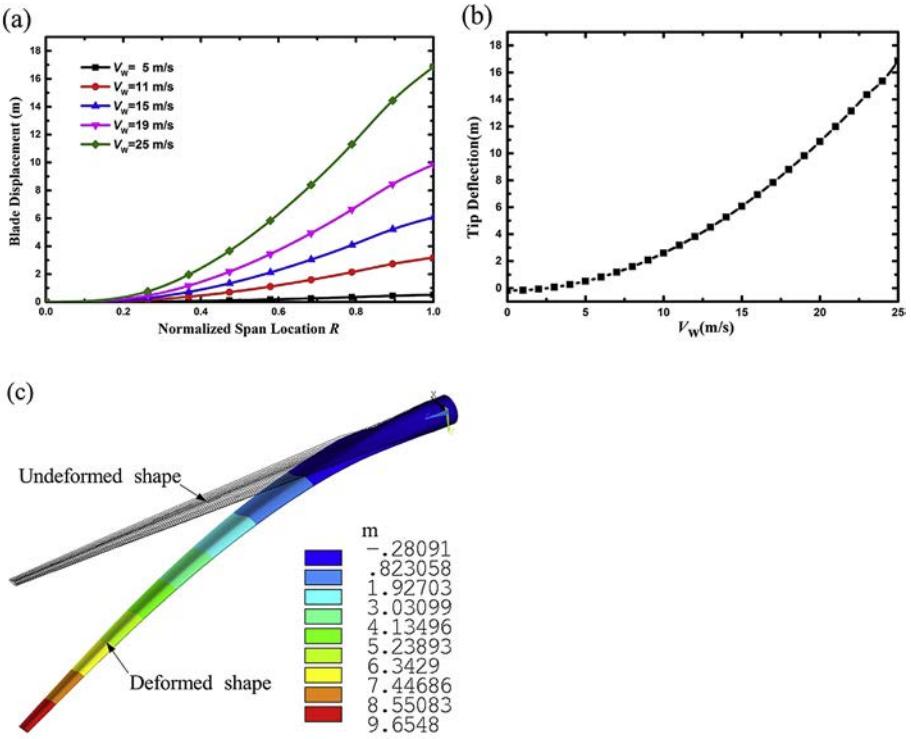

Fig. 2. Deformation of the blade in quasi-static simulations: (a) blade displacement along the blade length at five typical wind speeds; (b) tip deflections of the blade at wind speeds from 0 m/s to 25 m/s; (c) the overall structural deflection of the blade corresponding to the debonding initiation at V_w = 19 m/s.

$$v_{res} = \sqrt{v_w^2(1-a)^2 + v_b^2(1+a')^2} \tag{14}$$

where a and $a\prime$ are the axial and tangential induction factors, respectively; and local blade speed v_b was calculated by:

$$v_b = wr \tag{15}$$

and

$$\omega = \frac{v_w T_{TSR}}{R} \tag{16}$$

where ω, r, and R are the rotation angular speed of the blade, the distance of the blade segment from the rotation center, and the radius of the wind turbine, respectively. T_{TSR} is the tip speed ratio, which was assumed to have a constant value of 7 [20]. It should be noted that the aerodynamic forces are affected by the blade deformation when in service. Since the focus of this study is on the damage prediction modeling of the blade, the aerodynamic loads were assumed independent of the blade deformation and the aeroelastic effects were ignored. The centrifugal force, F_C, was defined by:

$$F_C = m_r \omega^2 r \tag{17}$$

here, m_r is the mass of the blade segment. The gravitational force, F_G, was defined by:

$$F_G = m_r g \quad (18)$$

here, g is the gravitational constant. In order to increase the effective loading to cause flap-wise bending, the gravitational force F_G was assumed to act along the rotating direction of the blade (see Fig. 1).

3.1.2. Blade materials

The skin and spar of wind turbine blades are typically manufactured with many distinct laminated materials and sandwich panels. In order to simplify the blade model, it was assumed that the shell and spar were manufactured from the same multidirectional $[0/90/-45/+45]_s$ GFRP laminate with the thickness and density of 4 mm and 1800 kg/m^3 [20], respectively. An aluminum root joint with the thickness of 40 mm and density of 2700 kg/m^3 was glued to the composite laminates internally. A typical adhesive material was applied to the adhesive layers between the shell-spar joint and shell-root joint. The material properties of the blade structure and adhesive layers are listed in Tables 1–3.

3.2. Structural scale

The blade geometry generated by NuMAD was integrated within the simulation environment of ANSYS APDL. The meshing of the shell, spar and root was performed using higher-order 8-node SHELL281 elements in ANSYS APDL. The mesh size was chosen as 0.1 m basing on a consideration of the balance between accuracy and computational efficiency.

3.2.1. Damage modeling

In order to assess matrix micro-cracking and adhesive debonding in the rotor blade, the multi-scale progressive damage model and CZM depicted in Section 2.1 and Section 2.2 were applied to the FE model in both quasi-static and fatigue simulations. The laminate constitutive equations for the progressive damage model were implemented into ANSYS through a Fortran based USERMAT [45] to predict ply crack density and associated stiffness degradation for the laminate. Further details of the USERMAT has been illustrated in Ref. [20]. Perfect adhesion was assumed on the interfaces between the shell-spar adhesive layer and the shell-root joint. Debonding initiation and propagation in the adhesive layers were modeled by cohesive traction separation law. The adhesive layers were represented by contact elements 8-node CONTACT174 and 3D TARGE170, and delamination between the contact elements was referred to as debonding. The components of both contact gap and tangential slip distance have been used to define interfacial separation, which are computed through the type of contact element and the location of contact detection point.

3.2.2. Boundary conditions

Fixed boundary conditions were applied to the end of the shell and root joint to simplify the connections between the blade root and hub. Aerodynamic forces defined by Eq. (11) and Eq. (12) were applied at the blade segment aerodynamic centers through additional nodes, which were projected onto X-axes and Y-axes of the FE model through F_{Xi} and F_{Yi} ($i = 1, 2 \ldots 8$) shown in Fig. 1. Each of these nodes were selected as the master node for the rigid region on the corresponding blade segment skin panels, allowing for loading distribution on each segment. Furthermore, the centrifugal force F_C and gravitational force F_G were applied as acceleration body loads to the entire structure through the corresponding blade rotational speed ω and gravitational constant $g = 9.81$ m/s^2, respectively.

Table 1
Material properties for $[0/90/-45/+45]_s$ GFRP laminate used as the blade material of the shell and spar [20].

E_x^0 (GPa)	E_y^0 (GPa)	G_{xy}^0 (GPa)	ν_{xy}^0	G_{xz}^0 (GPa)	G_{yz}^0 (GPa)
23.72	23.72	9.07	0.3079	4.1	4.1

Table 2
Material properties for aluminum used in the root joint.

E (GPa)	ν
73	0.36

Table 3
Material properties for shell-root and shell-spar adhesive layers [44].

Properties	Adhesive
Normal strength, σ_{max}^n (MPa)	12.00
Tangential strength, σ_{max}^s (MPa)	26.00
Normal fracture energy, G^n (kJ/m^2)	1.85
Tangential fracture energy, G^s (kJ/m^2)	3.64

4. Results and discussion

The developed user-defined material subroutine was used to assess the concurrent effects of matrix micro-cracking and the debonding of the blade on its load-bearing capability under both quasi-static and cyclic loads. As the changing aerodynamic and gravitational forces are the main sources to produce cyclic loads on the blade, it is necessary to understand the wind speed distribution during the entire life service of the blade. However, the wind speed distribution is never steady and dependents on various factors such as local weather system, local land terrain, and the height of wind turbines. For above reasons, the Weibull distribution has been commonly used in the literature to describe wind speed frequency [6]. Furthermore, from an engineering design perspective, it is necessary to investigate the structural performance under the worst-case and near worst-case scenario. Therefore, two load cases were considered in this study to assess the damage of the blade under quasi-static and cyclic loads. First, the blade was assumed to be in a parked position with the brake released when a sudden wind with speed of V_W was imposed, where V_W varied from 0 m/s to 25 m/s based on a typical Weibull distribution. This represents a critical operating condition with potential external situations during service life, where quasi-static simulations were performed. Specially, the 25 m/s represents the extreme external situation such as strong gale winds during a storm. Second, considering that the debonding of the blade occurs at extreme loading condition [10,21], the blade was assumed to work in a moderate breeze when a near gale wind was imposed. The cyclic loading caused by the constantly changing of wind from a normal speed 7.5 m/s to an extreme speed of 15 m/s was applied to the blade in the fatigue simulations [6,20].

4.1. Quasi-static simulation

4.1.1. Overall structural deformation

To have a safe blade-tower-clearance, it is necessary to predict overall structural deformation of the blade. As shown in Fig. 2(a), the deformation of the blade was small at low wind speeds such as a moderate breeze; however, large deformation occurred when wind speeds increased to higher than 11 m/s. The tip deflection

increased nonlinearly with the increasing of wind speeds shown in Fig. 2(b). Here, the 25 m/s wind speed, representing the extreme external situation in fact, can cause the rotor blade structural collapse involved a combination of damage and failure modes. However, since the structural buckling and delamination were not considered in the developed model, the tip deflection at this loading case couldn't be predicted accurately. Specially, the overall structural deflection of the blade corresponding to the initiation of blade debonding (see Section 4.1.3) is shown in Fig. 2(c). The blade tip deflection reached 29.0% of the blade length, which was close to the value of 22.5% reported by a failure test for a 40 m long blade [21].

4.1.2. Matrix micro-cracking of the blade

The axial stress of the tension-side skin panel along the blade length, when the debonding initiated at wind speed of 19 m/s (see Section 4.1.3), is depicted in Fig. 3. The maximum axial stresses of the shell and spar were 634 MPa and 519 MPa, respectively, both of which occurred at the span-wise position of 6.1 m. The high stress regions of the shell and spar were located between spar webs as was expected. Note that the axial stress of the shell had a higher value at the geometrical transition region, where the root circular section transitioned to an airfoil shape at the maximum chord position. The analogous axial stress distribution along the blade was also observed by J. Montesano et al. [20] and C.L. Bottasso et al. [46]. The contours of the corresponding crack density for 90° plies were shown in Fig. 5(b) and Fig. 5(e). The peak crack densities of the shell and the spar reached 0.863 mm^{-1} and 0.866 mm^{-1} corresponding to the maximum axial stresses between the spar webs. Moreover, the peak +45° and −45° ply crack regions were located at the transition region of the blade (see Fig. 3). The damage distributions indicated that the transition region was the most critical region for matrix micro-cracking damage. This was observed by X. Chen et al. [10] through a failure test of a 52.3 m glass/epoxy composite blade, where it was reported that in this region a combined form of blade failure was observed.

Fig. 4(a) and Fig. 4(b) showed the peak crack densities for 90°, +45° and −45° plies of the shell and spar at wind speeds from 0 m/s to 25 m/s. For the tension-side panel of both the shell and spar, the micro-crack damage initiated at wind speeds of 11 m/s, which occurred much earlier than initiation of debonding as was expected. The values of peak micro-crack density subsequently increased rapidly to a clear plateau due to the increase of wind speed. The plateau was also found in the damage simulation for a 33.25 m length blade [20] and was observed as the significant of the delamination initiation for laminates [47]. However, after the crack initiation, the crack damage area grew slowly with the increasing of wind speed from 11 m/s to 14 m/s, and only 0.4% of the shell area and spar area were damaged at wind speed of 14 m/s shown in Fig. 4(c). When wind speed increased to higher than 14 m/s, the damage area increased rapidly, which reached values with 22.2% and 22.8% of the shell area and spar area, respectively, at wind speed of 25 m/s. This revealed that the crack damage initiation was dominated by the local concentration stress, while the crack damage propagation was dominated by the increase of the high stress region. The 90° ply crack density distribution is shown in Fig. 5. The crack damage initiated at the span-wise position 6.1 m, then, the ply crack propagated along the blade length due to the increasing of wind speed. The high crack density region, finally, was observed at span-wise position from 2 m to 15 m between the webs on the tension-side shell panel and spar cap at 25 m/s, where the peak density reached a high value of 1 mm^{-1}. Note that the debonding initiation of the shell-spar joint also occurred in this segment, and this region was experimentally reported as the most critical part for the ultimate collapse of the rotor blade [22].

4.1.3. Debonding of the blade

The debonding of the blade is considered as one of the major factors of the final collapse. The initiation and propagation of adhesive debonding under quasi-static load are shown in Fig. 6, which

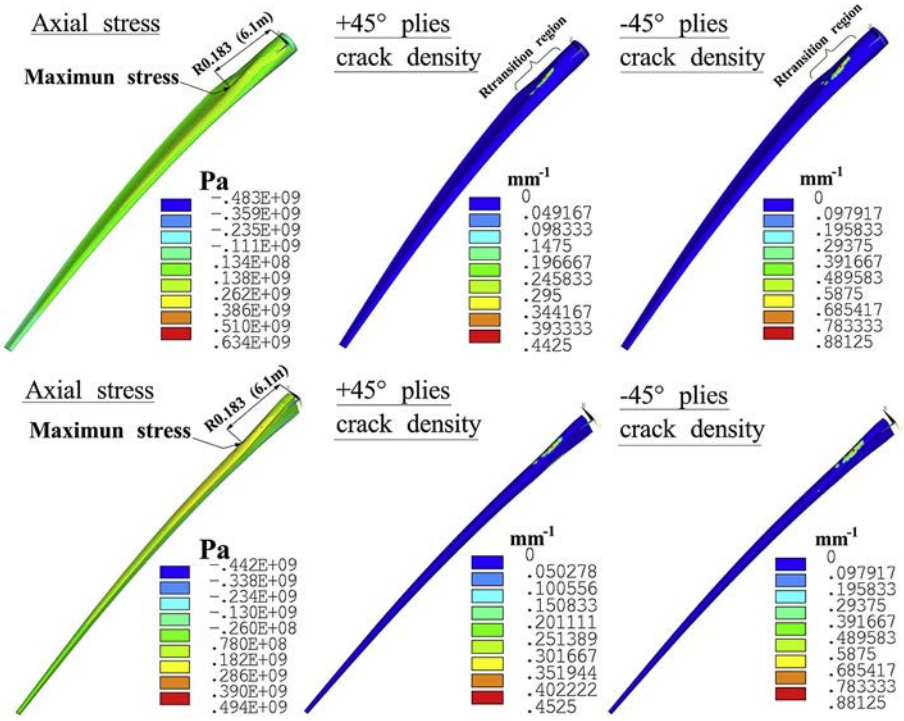

Fig. 3. Axial stress distribution of the tension-side skin panel along the blade length and ply crack density contours of +45° plies and −45° plies at $V_w = 19$ m/s.

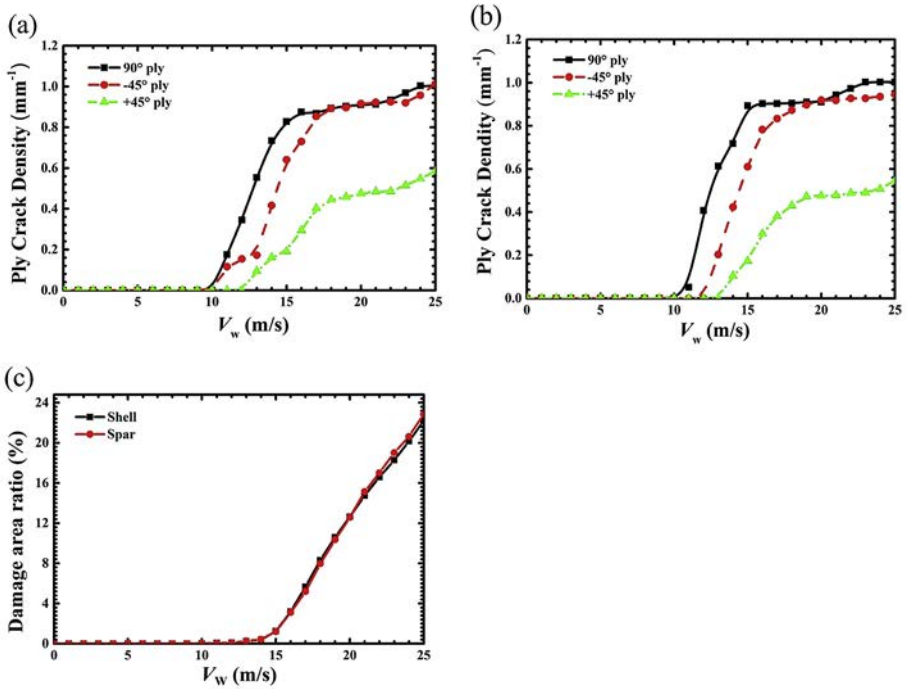

Fig. 4. Blade crack density evolution for 90°, +45° and −45° plies from 0 m/s to 25 m/s: (a) crack densities of tension-side shell panel at maximum stress location; (b) crack densities of tension-side spar cap at maximum stress location; (c) damage area to global area ratios of the shell and spar based on 90° ply crack damage.

is described by the damage parameter defined in Section 2.2. In the quasi-static simulation, debonding did not occur at low wind speeds, however, the shell-spar adhesive debonding initiated on the pressure side of the shell when wind speed increased to 19 m/s. This suggests that the strong winds such as gale and storm are likely to cause adhesive debonding of the blade. This damage mode was also experimentally observed to occur under extreme load, which was close to the ultimate collapse load [10,21]. The

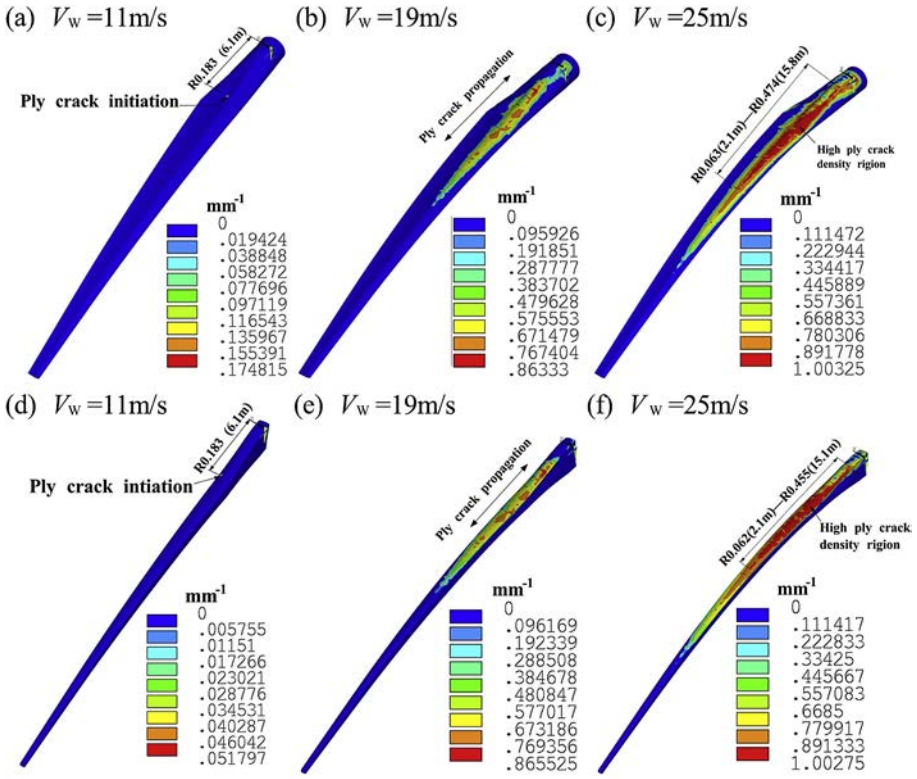

Fig. 5. The initiation and propagation of 90° ply crack damage on the shell and spar corresponding to V_w = 11 m/s, V_w = 19 m/s, and V_w = 25 m/s in quasi-static simulations.

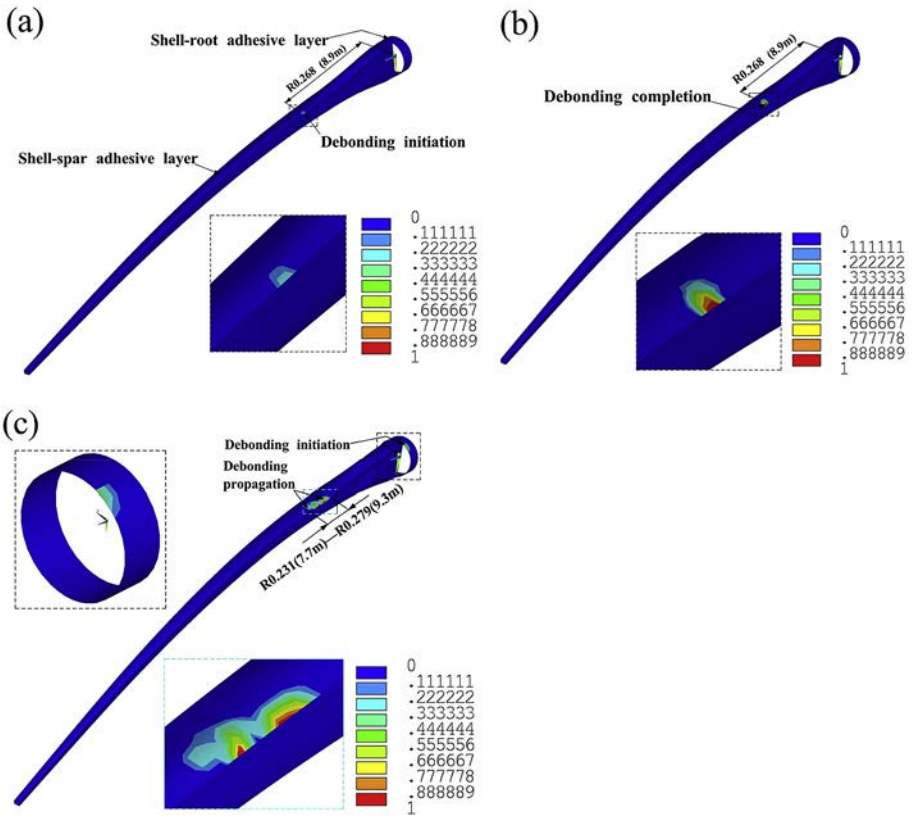

Fig. 6. Blade debonding contours of adhesive layers for adhesive 1 described by the damage parameter: (a) blade debonding initiation at $V_w = 19$ m/s; (b) blade debonding completion at $V_w = 22$ m/s; (c) blade debonding distribution at $V_w = 25$ m/s.

debonding initiation location was at the edge of the shell-spar adhesive joint with span-wise position 8.9 m, which was in the most critical span-wise segment reported in the full-scale test of a 34 m wind turbine blade [22]. After initiation, the adhesive debonding gradually propagated and completed at the same location (8.9 m) with the increasing of wind speed. As wind speed increased from 22 m/s to 25 m/s, the debonding zone expanded to the region between span-wise position from 7.7 m to 9.3 m. In addition, the shell-root adhesive joint also began to debond at the corner of the root at 25 m/s, which is the transition region of the spar and root.

To identify the initial debonding mechanism of the blade, the distributions of inter-laminar stresses in adhesive layers prior to debonding initiation of adhesive 1 were also investigated (see Fig. 7). As shown in Fig. 7(a), the mean normal stress in shell-spar adhesive layers was typically low due to compression of the spar, which was also reported by Y.M. Ji et al. [24]. However, the local normal stress was extremely high at the span-wise position 8.9 m, where the debonding initiated, and reached the cohesive peel strength. For shear stress, the maximum value occurred at the span-wise position 5.4 m instead of the debonding initiation location shown in Fig. 7(b). There is a strong possibility that the debonding initiation of shell-spar adhesive layer is dominated by the high local peel stress concentration, which is probably caused by the large localized non-linear bending. This result was reported in the full-scale test of a 40 m wind turbine blade [21]. For the shell-root adhesive layer, the maximum magnitude of the normal stress was only at 25.7% of the adhesive peel strength, while the shear stress was high and reached 72.3% of the adhesive shear strength shown in Fig. 7(c) and (d). The high shear stress regions were observed at the corners of the transition region of the spar and root, especially, the higher values occurred at the edge of the shell-root adhesive layer. This suggested that the extreme shear stress was likely the major cause for debonding initiation of shell-root adhesive layer.

4.2. Fatigue simulation

4.2.1. Progressive damage

Matrix micro-cracking damage contours for the fatigue simulation of the blade is shown in Fig. 8. After the first loading cycle, the matrix micro-cracking damage initiated in 90° plies of the tension-side skin panel for both the shell and spar with peak ply crack densities of 0.01625 mm^{-1} and 0.08125 mm^{-1}, respectively. As the loading cycle increased, the damage progressed along the length of the blade. Noted that similar to the static simulations the damage regions are also located between the webs, which are at the most critical span-wise region. After 6702 loading cycles, the local 90° ply crack densities of the shell and spar reached to a high level with values of 0.9325 mm^{-1} and 0.9125 mm^{-1}, respectively. As the progressive damage reduced the overall blade stiffness, the tip deflection increased and reached a plateau during the early stages of cycling, finally, a jump of the tip deflection occurred due to the debonding initiation by 6697 loading cycles (see Fig. 9). It should be noted that the damage doesn't imply the final catastrophic blade failure, however, the local damage with high ply crack density will eventually lead to local shell-spar adhesive debonding, which was also reported by B.F. Sorensen et al. [30].

4.2.2. Estimation of the remaining useful life

Performance evaluation is a key element in the development and maintenance of rotor blade. The remaining useful life (RUL) and

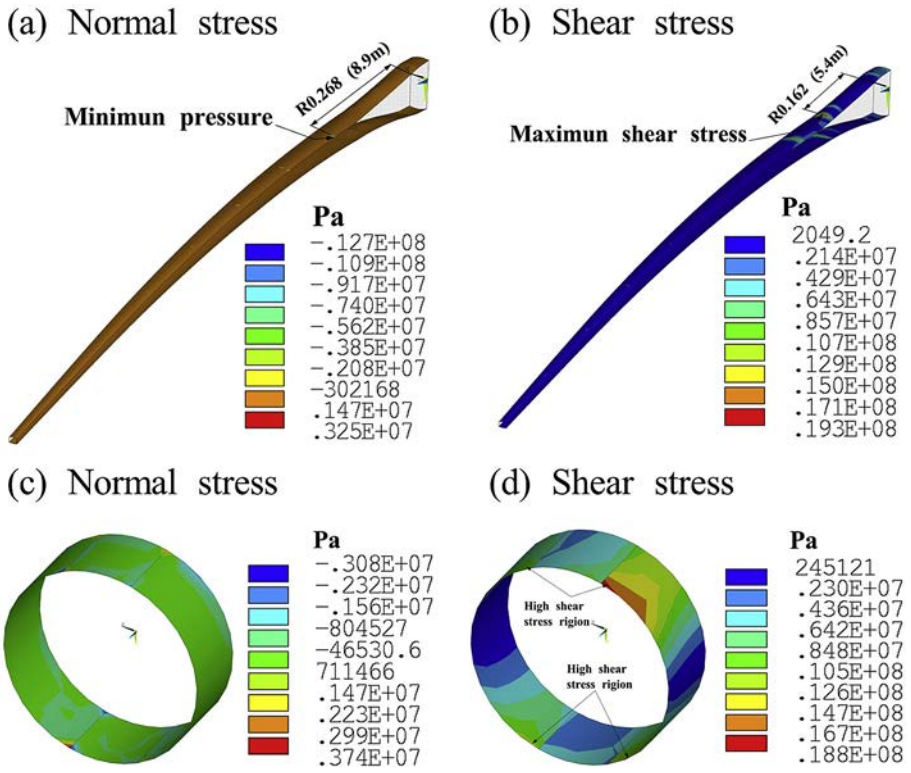

Fig. 7. Inter-laminar stresses of adhesive layers corresponding to the blade debonding initiation at V_w = 19 m/s.

maintenance of rotor blade and wind turbine systems have been modeled by many studies [48–50]. The developed multi-scale model provided a new method considering the matrix micro-damage and adhesive debonding to predict the RUL of the blade under cyclic loading conditions (see Fig. 10). The expected end of life (EOL) was defined as the cycles at which the debonding completion of the blade occurred, and the remaining useful life (RUL) of the blade was obtained as RUL = EOL-n, where n is the

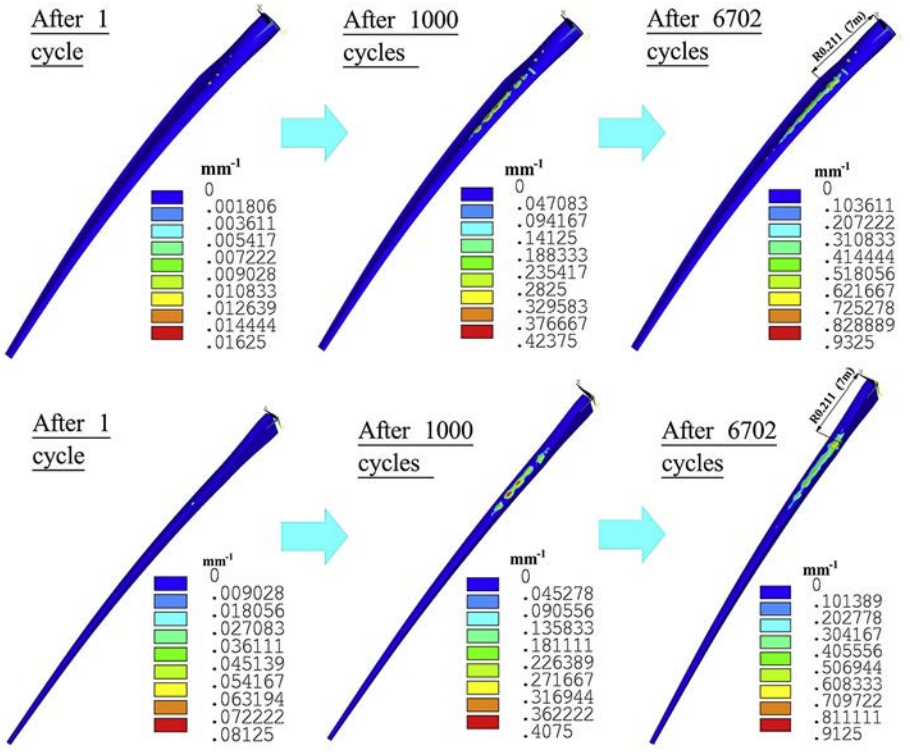

Fig. 8. The initiation and propagation contours of 90° ply crack densities for the shell and spar cycled between 7.5 m/s and 15 m/s.

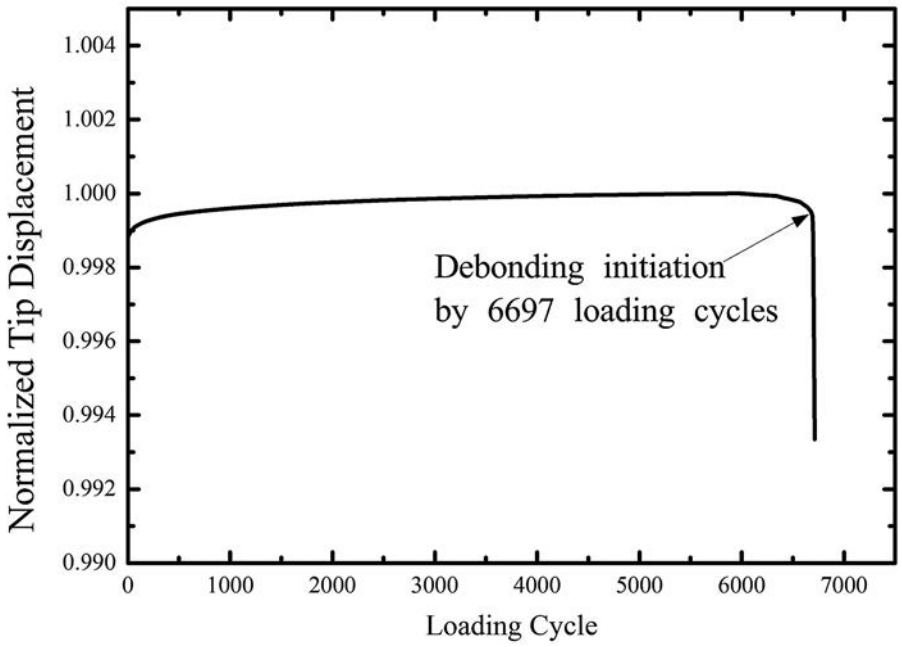

Fig. 9. Evolution of blade tip flap-wise normalized displacement under cyclic loading.

current cycle. Under the loading conditions of this study, the EOL was found to be 6702 cycles owing to the complete debonding of the shell-spar adhesive joint as depicted in Fig. 11. Since it has been well established that fatigue damage process is load-path dependent, this model can also be used to predict the progressive damage and the EOL of rotor blade under different fatigue loading cases including the realistic loading spectra. Moreover, results reveal that the matrix micro-cracking damage occurred during the early stage of RUL and became saturated for long lifetime (see Fig. 10). Then, at the end of the RUL the matrix micro-cracking increased rapidly to a critical value of the crack density. These results can be useful for developing appropriate maintenance plan for the blade.

4.2.3. Effects of progressive damage on debonding

The debonding contours of adhesive joints described by the damage parameter under cyclic loading are shown in Fig. 11(a)–(c). By 6697 loading cycles the debonding initiation occurred at the edge of shell-spar adhesive joint with span-wise position 7 m corresponding to the location of the maximum 90° ply crack density. This revealed that the local debonding may be caused by the high density of ply crack damage. After initiation, debonding completed by 6702 loading cycles, and thereafter the debonding zone propagated rapidly with the increasing of loading cycles at the edge of shell-spar adhesive layer along the blade length direction. In order to understand the influences of

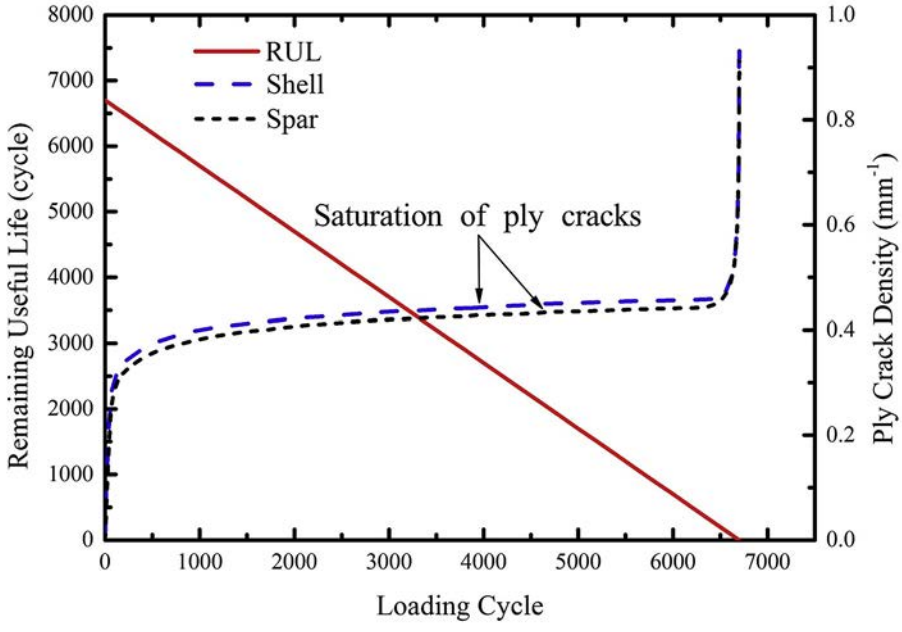

Fig. 10. Remaining useful life prediction of the blade and the maximum crack density for 90° under cyclic loading.

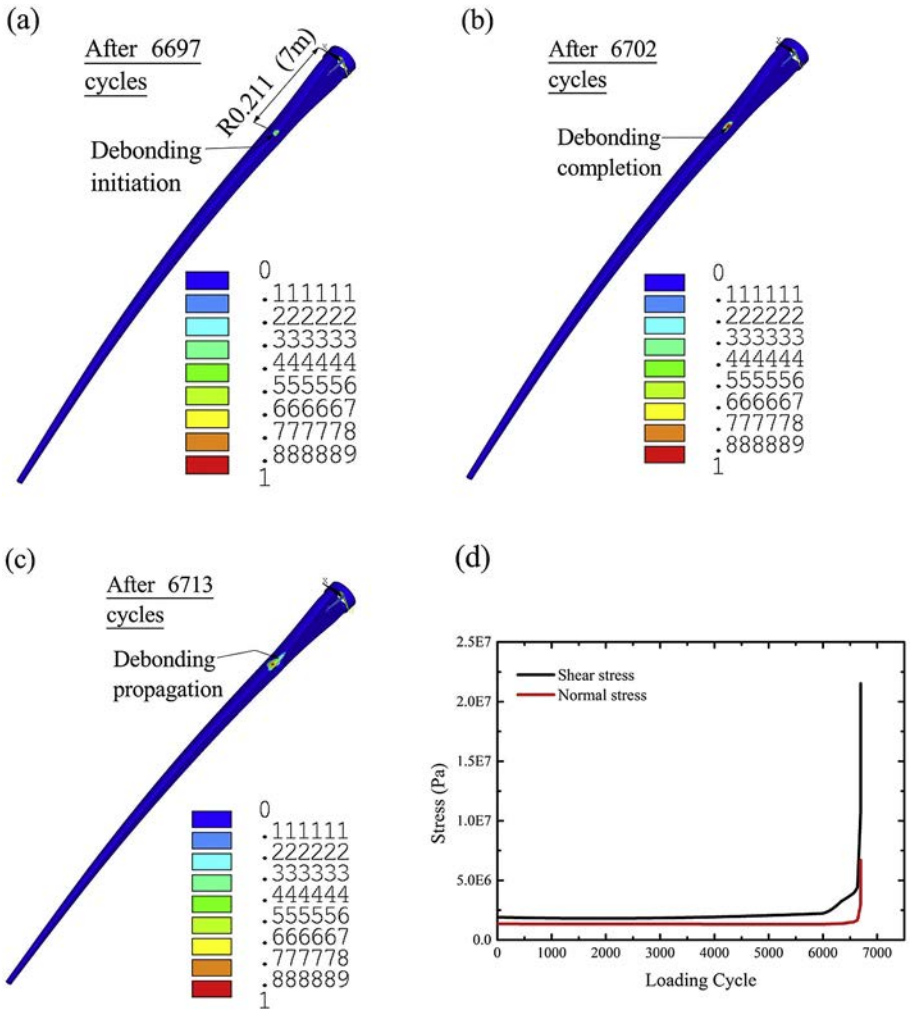

Fig. 11. Blade debonding contours described by the damage parameter and inter-laminar stresses contours of the adhesive layer under cyclic loading: (a) debonding initiation after 6697 cycles; (b) debonding completion after 6702 cycles; (c) debonding propagation after 6713 cycles; (d) normal and shear stresses of the adhesive layer at the debonding initiation location.

ply cracks on the debonding, the inter-laminar stresses of the adhesive layer at the debonding initiation location under cyclic loadings are shown in Fig. 11(d). The normal stress and shear stress increased progressively during the early stages of cycling due to the propagation of ply crack damage. After 6000 loading cycles, both of the normal stress and shear stress increased rapidly, and the debonding initiation criterion defined in Section 2.2 was reached by 6697 loading cycles when the corresponding 90° ply crack density reached the saturation of high density ply cracks. This high level of local ply crack density has been reported as the plateau of crack density in quasi-static studies, which has been experimentally observed to signify the onset of delamination for both multidirectional laminates and wind blade composite laminates [30,47]. Furthermore, the shear stress and normal stress reached, respectively, 82.8% of the adhesive shear strength and 55.8% of the adhesive peel strength at the debonding initiation location, which suggested that the shear stress was dominant for the debonding caused by progressive ply crack damage under cyclic loading.

4.3. Discussion

The developed multi-scale model is capable of predicting the progress damage and RUL of rotor blade accounting for the interaction of subcritical progressive ply cracking and structural joint adhesive debonding under quasi-static and cyclic loading conditions, which is useful for the design and maintenance of the rotor blade. The predictions suggest that saturation of ply cracks in critical regions of the blade cause structural joint adhesive debonding to initiate, which is consistent with the literature. The computationally calibrated damage-based model component minimizes the need to conduct additional costly experimental test, which is seen as an advantage. Nonetheless, some additional considerations are necessary to further improve the accuracy of the predictions. For instance, other key damage modes in wind turbine blades such as inter-ply delamination onset and global structural buckling of the blade components are not currently considered. Under service loads, compressive stresses may lead to delamination and structural buckling, and therefore must be considered. Moreover, it was assumed that the wind speeds, and thus the aerodynamic and centrifugal loading, were varying through constant peak values during the fatigue simulations. Realistic loading spectra based on reported wind speed data can also be applied to the model in order to optimize the blade design for a specific local land terrain.

5. Conclusions

In this study, a fully physical model accounting for matrix micro-cracking and adhesive debonding concurrently was developed to predict the progressive damage and RUL of wind turbine rotor blade under quasi-static and fatigue loading. The matrix micro-cracking damage was assessed by a multi-scale progressive damage model based on the synergistic damage mechanics, and the structural debonding was predicted by a CZM. The complete structure of the blade was considered including the shell-spar adhesive joint and shell-root adhesive joint. Overall, the developed model will be a useful tool in blade design and maintenance. The following conclusions can be reached from the present study:

(1) The simulation results clearly demonstrated the ability of the model to predict the co-effects of the combined damage modes in the blade structure under both quasi-static and fatigue loading, which is vital for increasing the accuracy of service life prediction and optimizing the design of the blade structure. Based on the model, the RUL of the blade can be predicted under different fatigue loading situations.
(2) For the quasi-static study, the blade tip deflection increased nonlinearly with increasing wind speeds, reaching 29.0% of the blade length at 19 m/s agreeing with the literature. The matrix micro-cracking occurred due to the local concentration stress and was mainly caused by high wind speeds (e.g., over 14 m/s), moreover, the adhesive debonding ultimately initiated at the shell-spar joint due to high local normal stress.
(3) For the fatigue study, sub-critical damage grew along the length of the blade due to the progressing of cyclic loading, and caused the increasing of normal stress and shear stress in adhesive layer. Moreover, the local damage with high ply crack density finally led to local shell-spar adhesive debonding.
(4) The geometrical transition region of the blade was observed to be the critical ply crack damage region under quasi-static and fatigue loading, which was found to be in agreement with the previous studies.

Acknowledgements

The authors thank the China Scholarship Council, the Natural Sciences and Engineering Research Council of Canada (NSERC), the Northwestern Polytechnical University, the University of Toronto, and the University of Waterloo for funding in support of this work. We would also like to express our gratitude to ANSYS and SimuTech for their support throughout this project.

References

[1] J. Wang, S. Qin, S. Jin, J. Wu, Estimation methods review and analysis of offshore extreme wind speeds and wind energy resources, Renew. Sustain. Energy Rev. 42 (2015) 26–42, https://doi.org/10.1016/j.rser.2014.09.042.
[2] Y. Feng, H. Lin, S.L. Ho, J. Yan, J. Dong, S. Fang, Y. Huang, Overview of wind power generation in China: status and development, Renew. Sustain. Energy Rev. 50 (2015) 847–858, https://doi.org/10.1016/j.rser.2015.05.005.
[3] G.M. Joselin Herbert, S. Iniyan, E. Sreevalsan, S. Rajapandian, A review of wind energy technologies, Renew. Sustain. Energy Rev. 11 (2007) 1117–1145, https://doi.org/10.1016/j.rser.2005.08.004.
[4] J. Chen, Q. Wang, W.Z. Shen, X. Pang, S. Li, X. Guo, Structural optimization study of composite wind turbine blade, Mater. Des. 46 (2013) 247–255, https://doi.org/10.1016/j.matdes.2012.10.036.
[5] G. Abumeri, F. Abdi, J. Paquette, Durability and reliability of large composite wind turbine blades, Sample J. 48 (2012) 7–14.
[6] M.M. Shokrieh, R. Rafiee, Simulation of fatigue failure in a full composite wind turbine blade, Compos. Struct. 74 (2006) 332–342, https://doi.org/10.1016/j.compstruct.2005.04.027.
[7] C.P. Chen, T.Y. Kam, Failure analysis of small composite sandwich turbine blade subjected to extreme wind load, Procedia Eng. 14 (2011) 1973–1981, https://doi.org/10.1016/j.proeng.2011.07.248.
[8] P. Brøndsted, H. Lilholt, A. Lystrup, Composite materials for wind power turbine blades, Annu. Rev. Mater. Res. 35 (2005) 505–538, https://doi.org/10.1146/annurev.matsci.35.100303.110641.
[9] W. Zhang, Z. Zhou, F. Scarpa, S. Zhao, A fatigue damage meso-model for fiber-reinforced composites with stress ratio effect, Mater. Des. 107 (2016) 212–220, https://doi.org/10.1016/j.matdes.2016.06.040.
[10] X. Chen, W. Zhao, X.L. Zhao, J.Z. Xu, Preliminary failure investigation of a 52.3m glass/epoxy composite wind turbine blade, Eng. Fail. Anal. 44 (2014) 345–350, https://doi.org/10.1016/j.engfailanal.2014.05.024.
[11] J.-S. Chou, C.-K. Chiu, I.-K. Huang, K.-N. Chi, Failure analysis of wind turbine blade under critical wind loads, Eng. Fail. Anal. 27 (2013) 99–118, https://doi.org/10.1016/j.engfailanal.2012.08.002.
[12] S.C. Tan, R.J. Nuismer, A theory for progressive matrix cracking in composite laminates, J. Compos. Mater 23 (1989) 1029–1047, https://doi.org/10.1177/002199838902301006.
[13] R. Talreja, Continuum modelling of damage in ceramic matrix composites, Mech. Mater 12 (1991) 165–180, https://doi.org/10.1016/0167-6636(91)90061-4.
[14] J.M. Whitney, On the “ply discount method” for determining effective thermoelastic constants of laminates containing transverse cracks, Compos. Part Appl. Sci. Manuf. 36 (2005) 1347–1354, https://doi.org/10.1016/j.compositesa.2004.11.012.
[15] C.V. Singh, R. Talreja, A synergistic damage mechanics approach for composite laminates with matrix cracks in multiple orientations, Mech. Mater 41 (2009) 954–968, https://doi.org/10.1016/j.mechmat.2009.02.008.
[16] J. Montesano, C.V. Singh, A synergistic damage mechanics based multiscale model for composite laminates subjected to multiaxial strains, Mech. Mater 83 (2015) 72–89, https://doi.org/10.1016/j.mechmat.2015.01.005.
[17] S. Shiri, M. Yazdani, M. Pourgol-Mohammad, A fatigue damage accumulation model based on stiffness degradation of composite materials, Mater. Des. 88 (2015) 1290–1295, https://doi.org/10.1016/j.matdes.2015.09.114.
[18] J.C. Marín, A. Barroso, F. París, J. Cañas, Study of fatigue damage in wind turbine blades, Eng. Fail. Anal. 16 (2009) 656–668, https://doi.org/10.1016/j.engfailanal.2008.02.005.
[19] H. Pollayi, W. Yu, Modeling matrix cracking in composite rotor blades within VABS framework, Compos. Struct. 110 (2014) 62–76, https://doi.org/10.1016/j.compstruct.2013.11.012.
[20] J. Montesano, H. Chu, C.V. Singh, Development of a physics-based multi-scale progressive damage model for assessing the durability of wind turbine blades, Compos. Struct. 141 (2016) 50–62, https://doi.org/10.1016/j.compstruct.2016.01.011.
[21] J. Yang, C. Peng, J. Xiao, J. Zeng, S. Xing, J. Jin, H. Deng, Structural investigation of composite wind turbine blade considering structural collapse in full-scale static tests, Compos. Struct. 97 (2013) 15–29, https://doi.org/10.1016/j.compstruct.2012.10.055.
[22] F.M. Jensen, B.G. Falzon, J. Ankersen, H. Stang, Structural testing and numerical simulation of a 34m composite wind turbine blade, Compos. Struct. 76 (2006) 52–61, https://doi.org/10.1016/j.compstruct.2006.06.008.
[23] Y. Hua, A.R.M. Kasavajhala, L. Gu, Elastic–plastic analysis and strength evaluation of adhesive joints in wind turbine blades, Compos. Part B Eng. 44 (2013) 650–656, https://doi.org/10.1016/j.compositesb.2012.02.001.
[24] Y.M. Ji, K.S. Han, Fracture mechanics approach for failure of adhesive joints in wind turbine blades, Renew. Energy 65 (2014) 23–28, https://doi.org/10.1016/j.renene.2013.07.004.
[25] H. Hosseini-Toudeshky, M. Jahanmardi, M.S. Goodarzi, Progressive debonding analysis of composite blade root joint of wind turbines under fatigue loading, Compos. Struct. 120 (2015) 417–427, https://doi.org/10.1016/j.compstruct.2014.10.025.
[26] H. Ghasemnejad, L. Occhineri, D.T. Swift-Hook, Post-buckling failure in multi-delaminated composite wind turbine blade materials, Mater. Des. 32 (2011) 5106–5112, https://doi.org/10.1016/j.matdes.2011.06.012.
[27] F. Cappello, D. Tumino, Numerical analysis of composite plates with multiple delaminations subjected to uniaxial buckling load, Compos. Sci. Technol. 66 (2006) 264–272, https://doi.org/10.1016/j.compscitech.2005.04.036.
[28] L.C.T. Overgaard, E. Lund, O.T. Thomsen, Structural collapse of a wind turbine blade. Part A: static test and equivalent single layered models, Compos. Part Appl. Sci. Manuf. 41 (2010) 257–270, https://doi.org/10.1016/j.compositesa.2009.10.011.
[29] R. Talreja, C.V. Singh, Damage and Failure of Composite Materials, Cambridge University Press, Cambridge; New York, 2012.
[30] B.F. Sorensen, E. Jorgensen, C.P. Debel, K.M. Halling, H.M. Jensen, T.K. Jacobsen, M. Jensen, K.M. Halling, Improved Design of Large Wind Turbine Blade of Fibre Composites Based on Studies of Scale Effects (Phase 1), RISO National Laboratory Report, Denmark, 2004.
[31] J. Montesano, C.V. Singh, Predicting evolution of ply cracks in composite laminates subjected to biaxial loading, Compos. Part B Eng. 75 (2015) 264–273, https://doi.org/10.1016/j.compositesb.2015.01.039.
[32] T. Sadowski, P. Golewski, M. Kneć, Experimental investigation and numerical modelling of spot welding–adhesive joints response, Compos. Struct. 112 (2014) 66–77, https://doi.org/10.1016/j.compstruct.2014.01.008.
[33] P.P. Camanho, C.G. Davila, M.F. de Moura, Numerical simulation of mixed-mode progressive delamination in composite materials, J. Compos. Mater 35 (2003) 1415–1438.

[34] D. Salimi-Majd, V. Azimzadeh, B. Mohammadi, Loading analysis of composite wind turbine blade for fatigue life prediction of adhesively bonded root joint, Appl. Compos. Mater 22 (2015) 269–287, https://doi.org/10.1007/s10443-014-9405-4.
[35] C.V. Singh, R. Talreja, A synergistic damage mechanics approach to mechanical response of composite laminates with ply cracks, J. Compos. Mater 47 (2013) 2475–2501, https://doi.org/10.1177/0021998312466121.
[36] R. Talreja, Stiffness properties of composite laminates with matrix cracking and interior delamination, Eng. Fract. Mech. 25 (1986) 751–762, https://doi.org/10.1016/0013-7944(86)90038-X.
[37] M. Elices, G.V. Guinea, J. Gómez, J. Planas, The cohesive zone model: advantages, limitations and challenges, Eng. Fract. Mech. 69 (2002) 137–163, https://doi.org/10.1016/S0013-7944(01)00083-2.
[38] G. Alfano, M.A. Crisfield, Finite element interface models for the delamination analysis of laminated composites: mechanical and computational issues, Int. J. Numer. Methods Eng. 50 (2001) 1701–1736, https://doi.org/10.1002/nme.93.
[39] D. Laird, Numerical manufacturing and design tool (NuMAD) user manual, Sandia National Laboratories, 2001.
[40] D.M. Somers, The S816, S817, and S818 Airfoils, US Department of Energy, 2004.
[41] B. Beltran, T. Ahmed-Ali, M. Benbouzid, High-order sliding-mode control of variable-speed wind turbines, IEEE Trans. Ind. Electron 56 (2009) 3314–3321, https://doi.org/10.1109/TIE.2008.2006949.
[42] D. Cárdenas, H. Elizalde, P. Marzocca, S. Gallegos, O. Probst, A coupled aeroelastic damage progression model for wind turbine blades, Compos. Struct. 94 (2012) 3072–3081, https://doi.org/10.1016/j.compstruct.2012.03.034.
[43] W. Duan, F. Zhao, Loading Analysis and Strength Calculation of Wind Turbine Blade Based on Blade Element Momentum Theory and Finite Element Method, IEEE, 2010, pp. 1–4, https://doi.org/10.1109/APPEEC.2010.5448929.
[44] B.F. Sørensen, S. Goutianos, T.K. Jacobsen, Strength scaling of adhesive joints in polymer–matrix composites, Int. J. Solids Struct. 46 (2009) 741–761, https://doi.org/10.1016/j.ijsolstr.2008.09.024.
[45] ANSYS v15.0 User Manual, ANSYS Inc., Cannonsburg, PA, 2011.
[46] C.L. Bottasso, F. Campagnolo, A. Croce, S. Dilli, F. Gualdoni, M.B. Nielsen, Structural optimization of wind turbine rotor blades by multilevel sectional/multibody/3D-FEM analysis, Multibody Syst. Dyn. 32 (2014) 87–116, https://doi.org/10.1007/s11044-013-9394-3.
[47] J. Lambert, A.R. Chambers, I. Sinclair, S.M. Spearing, 3D damage characterisation and the role of voids in the fatigue of wind turbine blade materials, Compos. Sci. Technol. 72 (2012) 337–343, https://doi.org/10.1016/j.compscitech.2011.11.023.
[48] M.A. Djeziri, S. Benmoussa, R. Sanchez, Hybrid method for remaining useful life prediction in wind turbine system, Renew. Energy (2017), https://doi.org/10.1016/j.renene.2017.05.020.
[49] B. Le, J. Andre, Modelling wind turbine degradation and maintenance: modelling wind turbine degradation and maintenance, Wind Energy 19 (2016) 571–591, https://doi.org/10.1002/we.1851.
[50] A. Froger, M. Gendreau, J.E. Mendoza, E. Pinson, L.M. Rousseau, Solving a wind turbine maintenance scheduling problem, J. Sched. (2017), https://doi.org/10.1007/s10951-017-0513-5.